



Observation and mitigation of image distortion in high-energy electron radiography

Hao-Qing Li¹ · Liang Sheng² · Chang-Qing Zhang¹ · Ying-Chao Du¹ · Zheng Zhou³ · Xiu-Feng Weng² · Jia-Hao Xiao^{4,5} · Hong-Qiao Yin² · Bin Sun² · Kun Wei² · Yang Li² · Bao-Jun Duan² · Yong-Tang Liu² · Yan-Hong Zhang² · Mei Zhang² · Yan Song² · Xiao-Dong Zhang² · Jun Liu² · Zhu-Ming Fu² · Qing Xu² · Xue Du¹ · Jian-Peng Gao¹ · Xin-Yi Wang² · Xin-Jian Tan² · Dong-Wei Hei²

Received: 3 December 2022 / Revised: 11 February 2023 / Accepted: 23 March 2023 / Published online: 26 June 2023

© The Author(s), under exclusive licence to China Science Publishing & Media Ltd. (Science Press), Shanghai Institute of Applied Physics, the Chinese Academy of Sciences, Chinese Nuclear Society 2023

Abstract

Image distortion caused by the angular misalignment of quadrupole magnets in high-energy electron radiography has been studied systematically. We propose that the distortion originates from the coupling of the electron motions in the transverse directions, based on a theoretical analysis and the transfer-matrix method. The relative angular rotation between the second and third magnetic quadrupoles was identified as the main contributor to image distortion. This was verified by both a beam-dynamics simulation and experiments. Different strategies to mitigate this image distortion are also explored, including magnets online tuning, higher beam energy and larger magnification factor. This study provides criteria for designing experiments and paves the way for achieving higher image precision.

Keywords Misalignment · Angular rotation · Russian quadruplet · Transfer matrix

1 Introduction

High-energy density physics (HEDP) is the study of matter under extreme pressure and temperature conditions. Under these conditions, the hydrodynamic response results in a high expansion velocity of the order of microns per nanosecond. This therefore requires a diagnostic method with, simultaneously, a temporal resolution ranging from nanoseconds to picoseconds and a spatial resolution $< 1 \mu\text{m}$. Charged particle radiography has developed over decades [1–3]. High-energy electron radiography (HEER), one instance of this method, is attracting growing interest for its combination of potential high spatiotemporal resolution, accessibility, and ease of manipulation. HEER has been proposed for use in high-intensity heavy-ion accelerator facilities at the forefront of HEDP science [4, 5]. The basic idea of HEER is to use a set of magnetic quadrupoles to focus the scattered electrons passing through an object to form a point-to-point image on the detector plane. Since its proof-of-principle demonstration at the Los Alamos National Laboratory [6], significant efforts have been made to improve its performance, e.g., by introducing a higher-brightness electron source and an advanced electron-imaging optics design [7, 8]. The

This work was supported by the National Natural Science Foundation of China (Nos. 12005211 and 12075192).

✉ Liang Sheng
shengliang@tsinghua.org.cn

✉ Ying-Chao Du
dych@mail.tsinghua.edu.cn

✉ Zheng Zhou
z-zhou14@tsinghua.org.cn

¹ Department of Engineering Physics, Tsinghua University, Beijing 100084, China

² State Key Laboratory of Intense Pulsed Radiation Simulation and Effect, Northwest Institute of Nuclear Technology, Xi'an 710024, China

³ Institute of Applied Electronics, China Academy of Engineering Physics, Mianyang 621900, China

⁴ Institute of Intelligent Machines, Hefei Institutes of Physical Science, Chinese Academy of Sciences, Hefei 230031, China

⁵ Zhongke Hefei Institutes of Collaborative Research and Innovation for Intelligent Agriculture, Hefei 231131, China

application of high-quality beams with a low-energy spread, low emittance, high brightness, and short bunch length generated by state-of-the-art S-band photoinjectors has made significant progress in pushing the spatial resolution to the micron level [9]. Recently, a pioneering high spatial resolution of $0.8\ \mu\text{m}$ was achieved with a radio-frequency (rf) thermionic cathode gun at the Institute of Modern Physics, which provides high-flux electron beams with a low-energy spread and ensures an excellent signal-to-noise ratio in the acquired images [10, 11].

Meanwhile, upgrading and optimizing the imaging system (for example, by using elaborately designed quadrupoles and cascaded image units) also play an important role in achieving better spatial resolutions and expanding the scope of application [12, 13]. In particular, the use of a permanent magnet quadrupole (PMQ), with its appealing high gradient, allows a shorter focal length. This is beneficial for making the entire imaging system more compact and increasing the magnification factor [14–16]. Additional advantages are its lower cost, non-restriction from the thermal effect, and fluctuation of current [17, 18]. However, drawbacks of PMQs include demagnetization by radiation, stronger higher-order multiple fields, and sensitivity to misalignment, which degrade image accuracy and even cause serious deterioration of the image quality [19–21]. For example, image skewing was observed at the University of California Los Angeles (UCLA) when using a 4 MeV electron beam focused by a PMQ triplet [22]. Mitigating these defects is therefore crucial to further improve image quality.

In this paper, we report on the image distortion caused by the angular misalignment of PMQs in the Russian quadruplet (RQ) system, and propose strategies to mitigate it. Section 2 presents the experimental design and the observed phenomena. Their possible explanations are discussed and, eventually, identified as PMQ misalignment. Section 3 analyzes the origin of the distortion using the transfer matrix and performs start-to-finish simulations to validate the analysis. We also evaluate the influence of different misalignment modes and provide an upper tolerance limit for misalignment. Section 4 demonstrates the feasibility of online tuning to correct misalignments in simulations and experiments. Finally, the impacts of different factors in optical design, including the field gradient, beam energy, and magnification, are discussed and strategies are proposed accordingly.

2 Experiment design and results

The experiment was performed using the Xi'an 120 MeV linear accelerator. Electron beams with tunable time structures were generated in an S-band photocathode rf-gun and then accelerated by two 3-m-long traveling-wave accelerating tubes. The energy was tunable from 30 to 120 MeV.

A set of electromagnetic quadrupoles and correctors were used to focus and match the beam [23]. Beams with a 400 pC bunch charge, 10 ps pulse duration, 1 mm-mrad normalized emittance, and 0.1% energy spread were obtained at the entrance of the imaging system chamber. The imaging system consisted primarily of a quadruplet, as commonly used in HEER for its convenience in achieving equal focal lengths and magnifications in the x - and y -directions [24, 25]. An aperture placed in the Fourier plane, where the scattering angle was transformed into a transverse distribution, blocked electrons with a larger scattering angle, resulting in a lower transmittance in the image plane. A $100\ \mu\text{m}$ -thick high-resolution yttrium-aluminum-garnet (YAG) screen was used to convert the electron profile distribution to a visible-light image. The image was reflected onto a lens-coupled CCD placed perpendicular to the beamline using a mirror to avoid radiation damage. All the imaging system equipment (except the lens-coupled CCD) was placed in a vacuum chamber as shown in Fig. 1.

The imaging optics used in our experiment were similar to those in [14], where four PMQs were used to form a RQ. Unlike the two sets of PMQs with different gradients and magnet lengths used in Ref. [14], our experiment used identical gradients for all the PMQs, thereby facilitating the fabrication process and ensuring better uniformity. As their gradients are fixed, the PMQ positions become the only tunable parameters. These were optimized using the high-order beam transport code COSY INFINITY [26], which describes the fringe field using a six-parameter Enge function. In the experiment, the parameters were adjusted using several remote-controlled custom stages with micron-level precision. The parameters for a 30 MeV beam energy and magnification factors -1.85 and -1.96 in the horizontal and vertical planes, respectively, are listed in Table 1. The positions were calculated from the center of the magnet to the object plane.

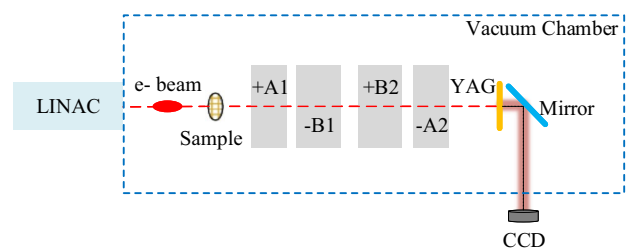


Fig. 1 (Color online) Schematic of the experiment setup. Electrons penetrating the sample are focused by four PMQs placed antisymmetrically with their focusing direction alternating, as denoted by $\pm A/B$, where \pm denotes focusing or defocusing and A/B represents PMQs with different lengths. The point-to-point image is formed on the YAG screen and then deflected to the camera by a mirror

Table 1 RQ parameters used in the experiment with 30 MeV electrons

Parameter	Length (mm)	Gradient (T/m)	Position (mm)
A1	13.47	191.4	22.4
B1	20.15	-186.8	49.3
B2	20.12	188.9	97.3
A2	13.64	-189.4	124.3

Simulations were performed before the experiments to validate the effectiveness of the optimized parameters. A Monte Carlo simulation of electrons penetrating a standard 100-mesh copper transmission electron microscopy (TEM) grid (pitch width 300 μm, hole width 260 μm, and bar width 40 μm) with a thickness of 50 μm was performed using GEANT4 [27]. The ASTRA code [28] was employed to conduct a beam-tracking simulation of the imaging system using the measured PMQ field maps. With a 0.2 mm radius collimator placed in the Fourier plane, a clear magnified image of the grid is expected, as shown in Fig. 2a, 120.84 mm downstream of A2. This result confirms the formation of the point-to-point image of an object.

However, there are always discrepancies between the experimental and ideal designs. After fine-tuning the beam and the quadrupole positions, a representative single-shot image was obtained in the experiment, as shown in Fig. 2b. The image is clear and some small contaminants are discernible. In spite of not applying a collimator in the experiment, the small magnet apertures worked equivalently to form an image contrast. On the other hand, the image is rotated clockwise by approximately 30° and the magnification factors are -2.26 and -3.06 in the horizontal and vertical planes, respectively.

As mentioned previously, some common factors may cause image distortion. Here, we present how these were eliminated in the experiment. First, because the distortion of

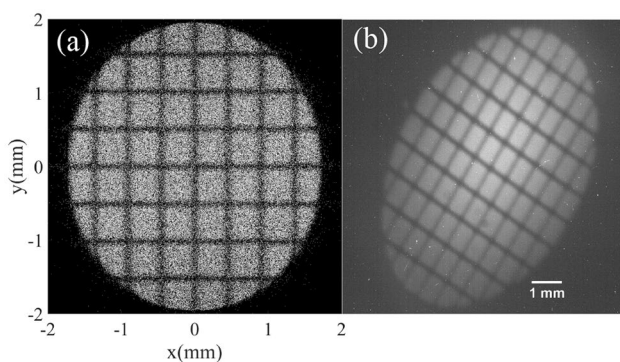


Fig. 2 Beam pattern in the image plane: **a** simulation and **b** experiment

our pattern appears similar to that observed at UCLA [22], the possibility of sample misplacement had to be excluded. Therefore, the sample was carefully checked before and after shooting to ensure it was set perpendicular to the beam longitudinal axis. We also tested deliberately orienting the grid at an angle of up to ± 20° relative to the transverse plane of the beamline. The measurements showed that the leaning direction was independent of the sample rotation, thus excluding the possibility of image distortion induced by sample rotation, as shown in Fig. 3. Second, the light path of the image-collecting system (including the mirror- and the lens-coupled CCD) was calibrated before conducting the experiment by imaging a standard calibration grid marker. Third, a misalignment of the beam trajectory relative to the magnetic-field center blurs and shifts the image. Hence, a HeNe laser copropagating with an electron beam was used to prealign the sample and quadruplet along the beamline axis. This was further mitigated by comparing the beam positions when the PMQs were moved into and out of the beamline individually, since the beam will experience a transverse kick when the beam trajectory deviates from magnetic center of the PMQs. In addition, optics calculations predicted unequal magnification along the perpendicular axes. Although the predicted effect is not as prominent as we observed, it causes image stretching instead of rotation.

Angular misalignment arises because the quadrupole magnetic field has only two symmetry planes, in contrast to the circular symmetrical field of a solenoid (round lens).

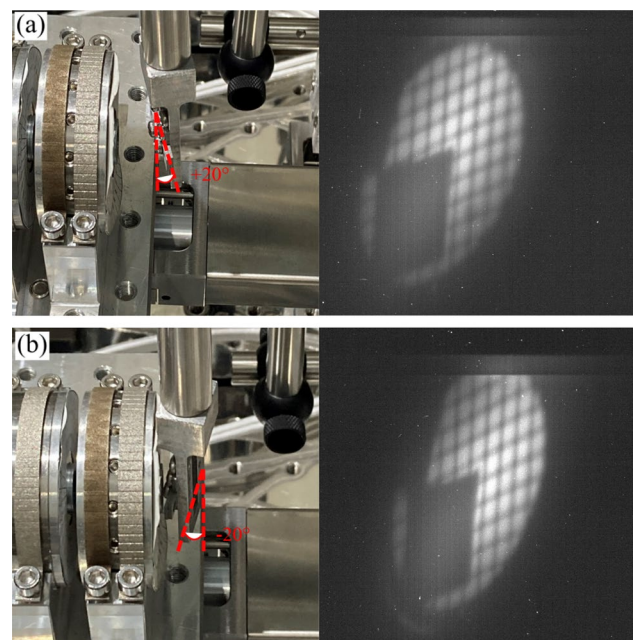


Fig. 3 (Color online) Images of the target rotated by 20° **a** counter-clockwise and **b** clockwise. A square copper patch in the lower-left region is imaged as a rhombus on the screen

Furthermore, the small PMQ aperture (8 mm in the present case) causes manufacturing, measurement, and alignment difficulties. Typically, the error in the magnetization direction of the magnet segments is approximately $\pm 1^\circ$ in manufacturing. The measurement error of the magnetic field is on the same scale, limited by the size of the Hall probe. Angular misalignment between the quadrupoles causes changes in the force experienced by the particle, making its trace change in consequence. The following section tests this hypothesis by investigating the influence of angular misalignment on radiography.

3 Theoretical analysis and simulation

A simple example of PMQs with angular misalignment is presented in Fig. 4.

The transfer matrix of a quadrupole magnet with angular rotation θ can be written

$$M_\theta = R_{-\theta} M_0 R_\theta, \tag{1}$$

with

$$M_0 = \begin{pmatrix} \cos KL & \frac{\sin KL}{K} & 0 & 0 \\ -K \sin KL & \cos KL & 0 & 0 \\ 0 & 0 & \cosh KL & \frac{\sinh KL}{K} \\ 0 & 0 & K \sinh KL & \cosh KL \end{pmatrix},$$

$$R_\theta = \begin{pmatrix} \cos \theta & 0 & \sin \theta & 0 \\ 0 & \cos \theta & 0 & \sin \theta \\ -\sin \theta & 0 & \cos \theta & 0 \\ 0 & -\sin \theta & 0 & \cos \theta \end{pmatrix},$$

where $K^2 = G/B\rho$, $B\rho$ is the magnetic rigidity related to the charge-mass ratio and the particle energy, G is the field gradient, and L is the effective magnetic field length of the PMQ. Since $\theta \ll 1$, Eq. 1 can be rewritten as

$$M_\theta = M_0 + \theta \Delta M,$$

where

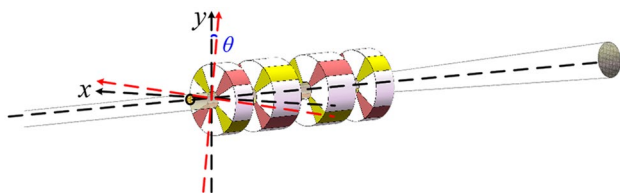


Fig. 4 (Color online) Magnetic field axis (red dashed arrows) orientation of the first magnet, with azimuthal angle θ relative to the beam transverse axis (black dashed arrows)

$$\Delta M = \begin{pmatrix} 0 & M_x - M_y \\ M_y - M_x & 0 \end{pmatrix}. \tag{2}$$

M_x and M_y are the upper-left and lower-right 2×2 matrices of M_0 , respectively. The entire transfer matrix of the RQ system with the i th magnet rotated by θ is obtained as

$$M_\theta^{\text{total}} = M_0^{\text{total}} + \theta M_{1-M_i} \Delta M_i M_{M_i-O}. \tag{3}$$

Here, M_0^{total} is the total transfer matrix without misalignment, M_{M_i-O} is the transfer matrix from the object plane to the i th magnet, and M_{1-M_i} is the transfer matrix from the i th magnet to the image plane. A similar result can be obtained computationally in more complex situations. The matrix shows that the electron motions in the x - and y -directions are coupled, yielding nonzero upper-right and lower-left matrix elements (in particular M_{13} and M_{31}) and causing image rotation and blurring.

Simulations of the rotated PMQs were performed to verify this prediction. For simplicity, we first considered a situation in which only magnet B1 was rotated by an angle θ ranging from 1° to 5° . The results are presented in Fig. 5.

The evolution of the image was reasonably consistent with the experimental results. Distortion arises rapidly with an increase in θ , and the image is barely recognizable when θ reaches 5° . However, an incongruity remains in so far as the mesh is a rhombus in the simulation but rectangular in the experimental results, as shown in Fig. 2b. This was because the sample shown in Fig. 2b is set with a rotation

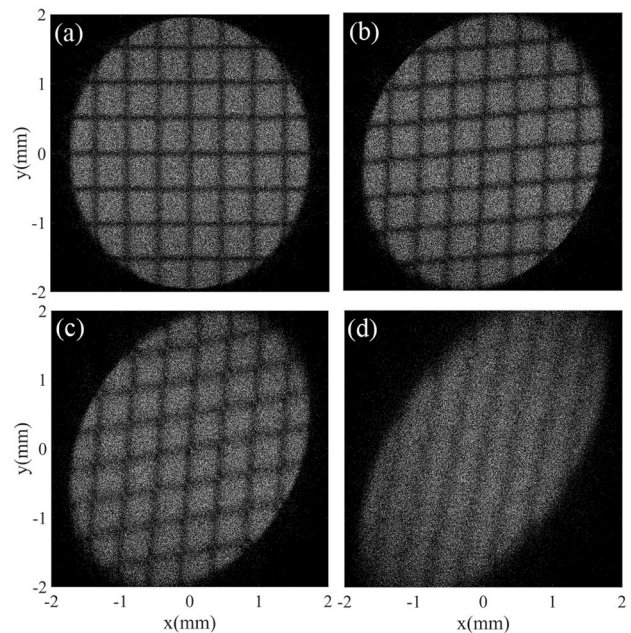


Fig. 5 Image rotation increases with the rotation angle of PMQ B1: **a** $\theta = 0^\circ$, **b** $\theta = 1^\circ$, **c** $\theta = 2^\circ$, **d** $\theta = 5^\circ$

that coincides with the direction of the image rotation, as can be verified by comparison with Fig. 3.

We next discuss the upper limit of the acceptable misalignment for the purpose of guiding experimental design. The angular misalignment of each magnet, despite being random, can be represented in terms of seven modes for the RQ system. The direction of rotation is denoted ‘N’ (clockwise) or ‘P’ (counterclockwise), as listed in Figs. 6 and 7, where each letter represents a magnet from A1 to A2 corresponding to Fig. 1b. The rotation angle of the image is defined as ϕ to quantify the rotation level:

$$\phi = \arctan \frac{y_{\text{rot}}}{x_{\text{rot}}} - \arctan \frac{y}{x}, \tag{4}$$

where $(x_{\text{rot}}, y_{\text{rot}})$ is the distorted position and (x, y) is the unperturbed position. With the expanded expressions in Eq. 2 (which can be derived computationally), $y_{\text{rot}}/x_{\text{rot}}$ is coupled in the x and y directions. This results in ϕ varying in different directions, which explains why the stripes are non-perpendicular to each other, as illustrated in Fig. 5. To compare the influence of different magnet rotations, the image rotation ϕ in the x - and y -directions of the different modes was calculated, as depicted in Fig. 6.

The most significant influence is displayed by the ‘PPNN’ and ‘NPNN’ modes. Setting the image rotation, shown in Fig. 5b, as the upper limit, the acceptable angular misalignment of this RQ system becomes $\pm 0.5^\circ$, since only B1 with a 1° rotation is equivalent to the ‘NPNN’ mode with a 0.5° rotation. A comparison of the first four modes shows that B1 and B2 have a stronger impact. This is reasonable, considering their greater lengths. Upon closer inspection, the image rotation is very sensitive to the relative rotation between B1 and B2, in all of these cases. On the other hand, they

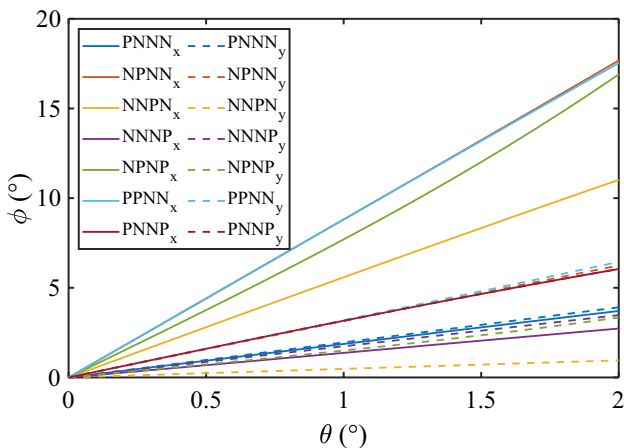


Fig. 6 (Color online) Relation between ϕ and θ for different angular misalignment modes. Solid lines represent ϕ in the x -direction and dashed lines in the y -direction

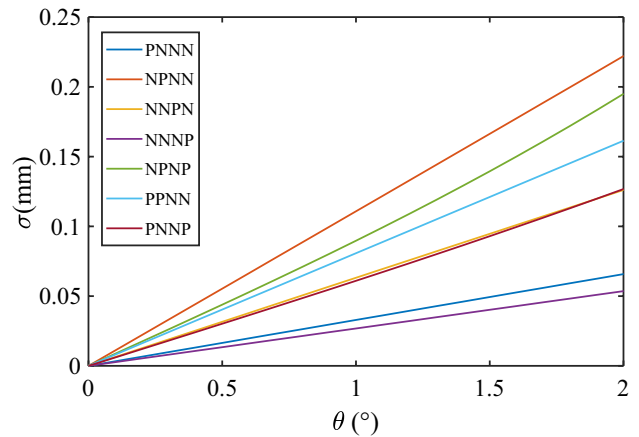


Fig. 7 (Color online) Relation between σ and θ for different angular misalignment modes

all show a larger ϕ in the x -direction than in the y -direction except for the ‘PNNN’ and ‘NNNP’ modes. This indicates that setting the concerned feature of the target along with the y -direction is recommended to minimize the detriment.

To estimate the image blur quantitatively, the image error σ is defined as

$$\sigma = \frac{\sum_{n=1}^N \sqrt{\frac{(x_{\text{rot}}-x)^2+(y_{\text{rot}}-y)^2}{x^2+y^2}}}{N}, \tag{5}$$

where N denotes the number of electrons in the beam pulse. The relationship between σ and θ for different modes is shown in Fig. 7.

A clear trend shows the image error σ increasing almost linearly with θ . Setting the value of σ , as shown in Fig. 5b, as the upper bound to judge the recognizability of the image, the tolerance of the entire RQ system becomes $\pm 0.5^\circ$. To verify the reliability of the analysis, we simulated the two most complicated misaligning modes, ‘NPNP’ and ‘PNNP’, with θ as their upper limit, as shown in Fig. 8. As expected,

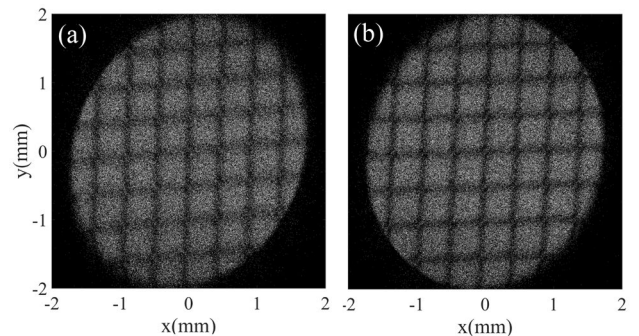


Fig. 8 Distorted image of **a** the NPNP mode with $\theta = 0.65^\circ$ and **b** the PNNP mode with $\theta = 0.95^\circ$

this image is similar to that in Fig. 5b, and the image on the right shows a weaker rotation, since the ‘PNNP’ mode has a lower growth in ϕ , as apparent in Fig. 6.

4 Strategies for mitigating the influence of angular misalignment

4.1 Online correction

Given the unavoidability of fabrication, assembly, and measurement defects, we here discuss possible remedies for these experiments. The above analysis identified the relative rotation between B1 and B2 as the most significant factor. This provides clues for mitigating the influence of angular misalignment. In the experiment, the beam pattern is monitored instantaneously using a lens-coupled CCD. PMQs can be moved in and out of the beamline by stages with a precision as high as $1\ \mu\text{m}$. When only one magnet is present in the beamline, a fine-tuned beam with a round profile originating from the LINAC is stretched in the defocusing direction and compressed in the focusing direction of the quadrupole magnetic field. A good alignment of the second magnet with the first causes a change in the beam pattern, but the direction of stretching and compression remains constant (or exchanges). However, an angular misalignment between the two magnets causes a rotation of the directions. Therefore, the magnets can be adjusted by observing the evolution of the beam patterns as they move into the beamline individually to mitigate the angular misalignment.

This process was demonstrated by simulating changes in the beam pattern while only B1 remained in the beamline and all other parameters were set to their designed values. The results are shown in Fig. 9.

The beam pattern is oblique when B1 is initially rotated by 5° . After correcting for this angle, the beam pattern returns to the vertical orientation. This simulation yields an angular resolution better than 1° without a further evaluation of the images.

The image in Fig. 10 was obtained experimentally. Only a part of the beam pattern is captured owing to the limited YAG screen size. Figure 10a shows the beam pattern produced with only B1 present in the beamline and with the three other magnets displaced, immediately after the image in Fig. 2b was taken. The stretching direction leans leftward, confirming the existence of an angular misalignment.

A manual rotation of B1 rotates the stretch direction clockwise. Owing to the lack of remote-controlled high-precision rotational stages, a corrected image of the TEM grid was not obtained in this experiment. However, the available results suffice to demonstrate its feasibility. By using an image processing program, a higher-precision correction is

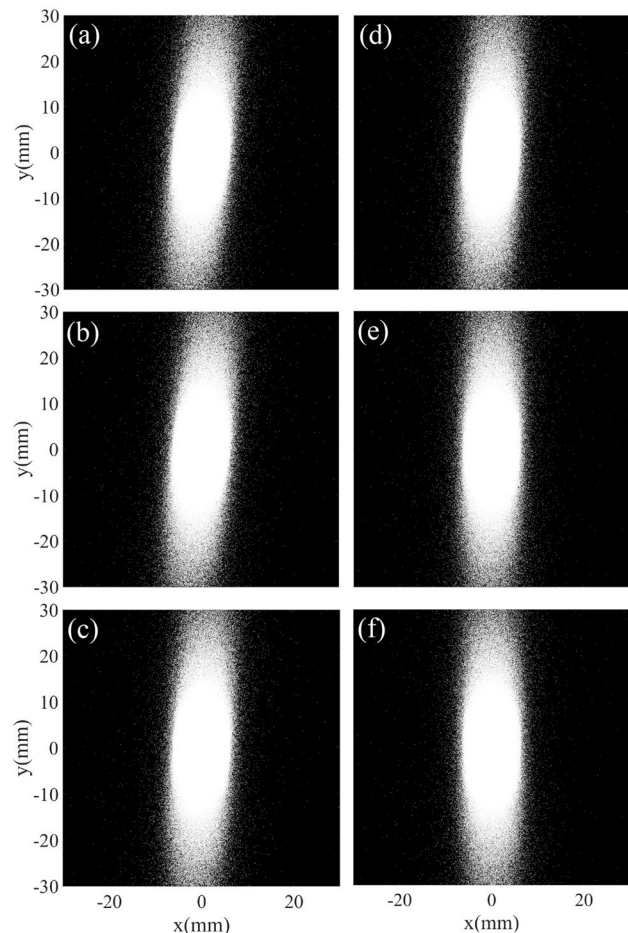


Fig. 9 Simulated beam pattern with only B1 present in the beamline. The rotation angle of B1 decreases from a 5° to 0°

achievable. However, that analysis and its practical application are beyond the scope of this study.

4.2 Higher beam energy

In addition to online tuning, the optimization of the optical design is crucial. The use of different beam energies enables the extraction of different target data, such as the mass density and the electromagnetic field strength [29, 30]. On the one hand, a wide gap between the magnets allows the convenient insertion of a collimator; on the other hand, a compact system is necessary when space is limited. Therefore, quadrupole spacings and lengths deserve due attention in experimental design. We investigated the influence of different factors on the angular-misalignment sensitivity of our system for a fixed magnification.

According to the expanded (computationally derivable) expressions in Eq. 3, the magnifications M_{11} and M_{33} remain constant when the magnet lengths and spaces are scaled inversely with K , which is proportional to the square root of

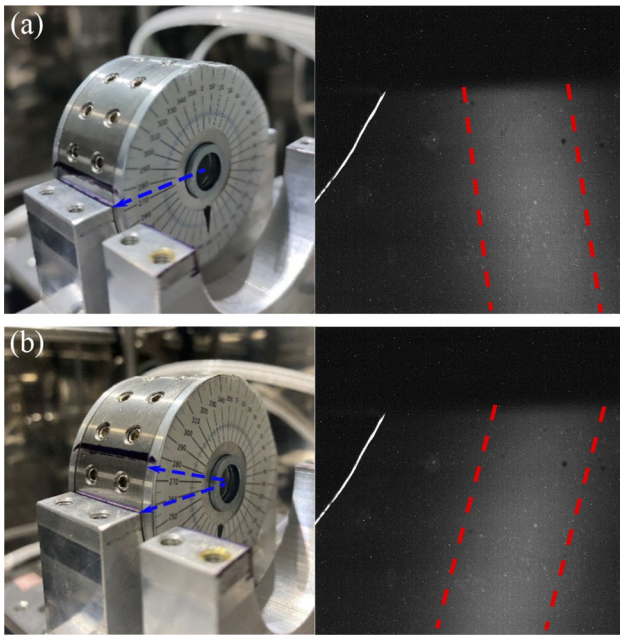


Fig. 10 (Color online) Beam pattern produced with only B1 present in the beamline. **a** The beam pattern leans leftward initially. **b** A clockwise rotation of magnet rotates the stretching direction of the pattern clockwise correspondingly. The bright curve on the YAG screen is caused by a crack

the field gradient when the beam energy is fixed. Furthermore, the error source factors M_{13} and M_{31} are related only to the rotation angle θ in this case. This indicates that image error σ is independent of the gradient. The same conclusion for the image rotation angle ϕ can be derived by a similar analysis. We verified the prediction with a numerical illustration by setting the beam energy to 30 MeV and fixing the magnification at -7.65 . The other parameters, including the lengths and distances, were recalculated and B1 was rotated by 1° to represent an error source. Figure 11 plots the image error σ and the image rotation angle ϕ as functions of the quadrupole gradient G . The independence of these quantities to the gradient allows greater flexibility in the optical design because the sensitivity to angular misalignment is not increased by the choice of the field gradient.

The same magnification can be achieved at different beam energies by tuning the object–image distance. The beam optics are redesigned accordingly to satisfy the requirement of a point-to-point image with a fixed magnification of -7.65 , using the same set of PMQs with gradient of 200 T/m in Fig. 11. We considered quadrupole B1 with a rotation angle of 1° to represent a distortion source. The image error σ and rotation ϕ , plotted in Fig. 12, show a rapid drop with increasing beam energy. However, the trend slows down substantially for energies beyond 200 MeV.

This also explains why the distortion in the case of a higher beam energy of 45 MeV with the same set of PMQs

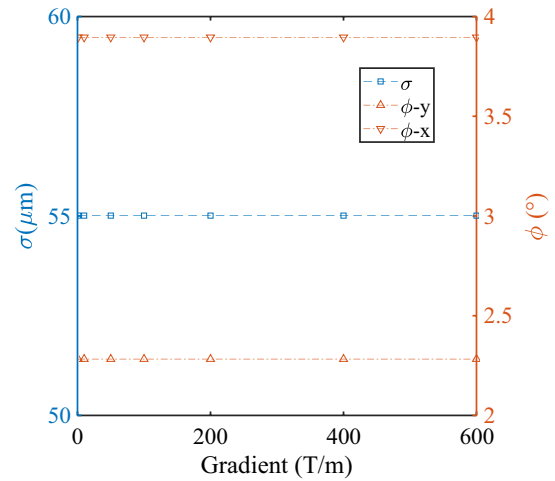


Fig. 11 (Color online) Image error and rotation plotted as functions of the gradient for a given beam energy and magnification. B1 was rotated by 1° to represent an error source

was not as apparent in previous experiments as in the present results [31]. Thus, a higher beam energy is recommended to mitigate the influence of misalignment in scenarios where the penetration ability is not a major factor.

4.3 Larger magnification

Different magnifications can be achieved using a given magnetic lens and beam energy by tuning the object distance and the image distance. This makes it convenient to locate the target and to zoom in to obtain a detailed characterization. Because the beam energy and lens parameters are fixed, M_{11} , M_{33} , M_{13} , and M_{31} are observed to be proportional to the

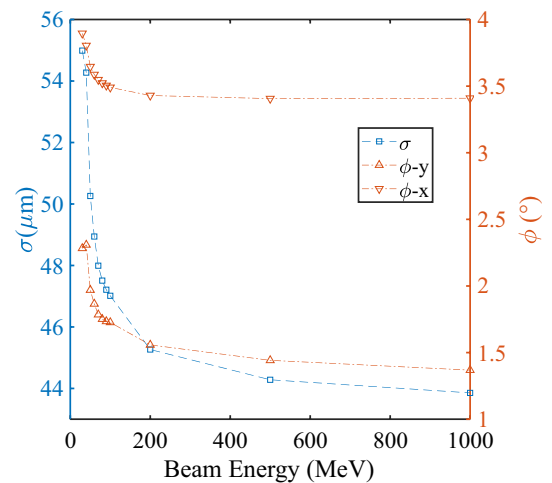


Fig. 12 (Color online) Image error and rotation plotted as functions of the beam energy, for a given set of PMQs and magnification. B1 was rotated by 1° to represent an error source

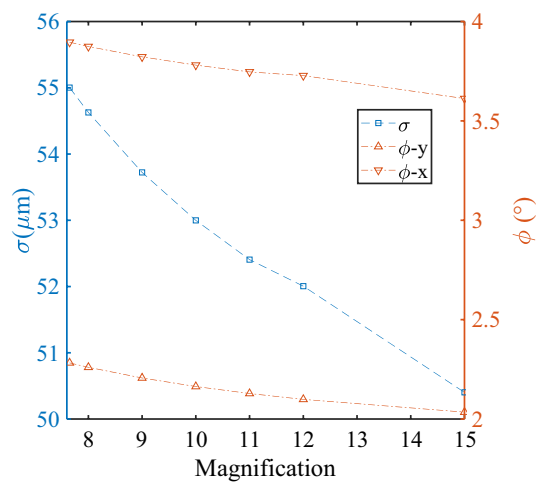


Fig. 13 (Color online) Image error and rotation plotted as functions of the magnification, for a given set of PMQs and beam energy. B1 is rotated by 1° to represent an error source

image distance. However, the absolute values of the coefficients in M_{11} and M_{33} are greater than M_{13} and M_{31} . Consequently, the numerator grows more slowly than the denominator of the term under the square root of Eq. 5. Thus, the image error decreases by increasing the image distance, which also increases the magnification. The dependences of the image error and rotation on the magnification, plotted in Fig. 13, validate the analysis. Hence a larger magnification is recommended.

5 Summary

In conclusion, the image distortion observed in PMQ-based high-energy electron radiography can be explained by the angular misalignment of PMQs, which leads to the coupling of electron motions in the x - and y -directions. Simulations and experiments validated our analysis, and the influence of different factors was studied in detail. Theoretical analysis shows that the relative rotation between B1 and B2 in an RQ system has the most significant impact. This motivates a more careful consideration of fabrication and assembly. In addition, limiting the angular misalignment of each quadrupole to $\pm 0.5^{\circ}$ is necessary to avoid fatal distortion. The feasibility of the online tuning of the magnets individually, based on the beam pattern, to correct the misalignment was verified experimentally. A higher beam energy and a greater magnification also help to mitigate the misalignment. In addition, the gradient analysis justifies the compacting of the imaging system without increasing the distortion. Further work, including the introduction of an image processing program and rotational stages, is required to achieve higher precision adjustments in future experiments. Most of the

considerations can be extended to designs utilizing different types of quadrupole systems. This method may be useful in other applications such as beam-based alignment and beam characterization [32, 33].

Acknowledgements The authors thank the staff of the Xi'an 120 MeV linear accelerator of the Northwest Institute of Nuclear Technology for their support during the experiments.

Author contributions All authors contributed to the study conception and design. Material preparation, data collection and analysis were performed by Hao-Qing Li, Liang Sheng, Chang-Qing Zhang, Ying-Chao Du, Zheng Zhou, Xiu-Feng Weng, Jia-Hao Xiao and Bin Sun. The first draft of the manuscript was written by Hao-Qing Li, Zheng Zhou, and all authors commented on previous versions of the manuscript. All authors read and approved the final manuscript.

Data availability The data that support the findings of this study are openly available in Science Data Bank at <https://www.doi.org/10.57760/sciencedb.08165> and <https://cstr.cn/31253.11.sciencedb.08165>.

Conflict of interest The authors declare that they have no competing interests.

References

1. N.S.P. King, E. Ables, K. Adams et al., An 800-MeV proton radiography facility for dynamic experiments. *Nucl. Instrum. Methods A* **424**, 84–91 (1999). [https://doi.org/10.1016/S0168-9002\(98\)01241-8](https://doi.org/10.1016/S0168-9002(98)01241-8)
2. A.A. Golubev, V.S. Demidov, E.V. Demidova et al., Application of TWAC beams for diagnostics of fast processes. *Atom. Energy* **104**, 134–141 (2008). <https://doi.org/10.1007/s10512-008-9004-2>
3. C.L. Morris, N.S.P. King, K. Kwiatkowski et al., Charged particle radiography. *Rep. Prog. Phys.* **76**, 046301 (2013). <https://doi.org/10.1088/0034-4885/76/4/046301>
4. Y. Zhao, R. Cheng, Y. Wang et al., High energy density physics research at IMP, Lanzhou, China. *High Power Laser Sci. Eng.* **2**, e39 (2014). <https://doi.org/10.1017/hpl.2014.44>
5. Q. Zhao, Y. Ma, J. Xiao et al., Three-dimensional high-energy electron radiography method for static mesoscale samples diagnostics. *Appl. Sci.* **9**, 3764 (2019). <https://doi.org/10.3390/app9183764>
6. F. Merrill, F. Harmon, A. Hunt et al., Electron radiography. *Nucl. Instrum. Methods B* **261**, 382–386 (2007). <https://doi.org/10.1016/j.nimb.2007.04.127>
7. F.E. Merrill, J. Goett, J.W. Gibbs et al., Demonstration of transmission high energy electron microscopy. *Appl. Phys. Lett.* **112**, 144103 (2018). <https://doi.org/10.1063/1.5011198>
8. Q.T. Zhao, S.C. Cao, R. Cheng et al., Generation of uniform transverse beam distributions for high-energy electron radiography. *Laser Part. Beams* **36**, 313–322 (2018). <https://doi.org/10.1017/s0263034618000265>
9. Z. Zhou, Y.C. Du, S.C. Cao et al., Experiments on bright field and dark field high energy electron imaging with thick target material. *Phys. Rev. Accel. Beams* **21**, 074701 (2018). <https://doi.org/10.1103/physrevaccelbeams.21.074701>
10. Y.L. Zhu, P. Yuan, S.C. Cao et al., Design and simulation of a LINAC for high energy electron radiography research. *Nucl. Instrum. Methods A* **911**, 74–78 (2018). <https://doi.org/10.1016/j.nima.2018.09.133>

11. Z.H. Ran, Z.P. Li, Q.T. Zhao et al., Demonstration of high energy electron radiography with sub-micron spatial resolution. *Nucl. Instrum. Methods A* **1015**, 165769 (2021). <https://doi.org/10.1016/j.nima.2021.165769>
12. M.S. Freeman, J.C. Allison, E.F. Aulwes et al., Dark field proton radiography. *Appl. Phys. Lett.* **117**, 144103 (2020). <https://doi.org/10.1063/5.0021044>
13. W. Wan, F.R. Chen, Y. Zhu, Design of compact ultrafast microscopes for single- and multi-shot imaging with MeV electrons. *Ultramicroscopy* **194**, 143–153 (2018). <https://doi.org/10.1016/j.ultramicro.2018.08.005>
14. Z. Zhou, Y. Fang, H. Chen et al., Demonstration of single-shot high-quality cascaded high-energy-electron radiography using compact imaging lenses based on permanent-magnet quadrupoles. *Phys. Rev. Appl.* **11**, 034068 (2019). <https://doi.org/10.1103/PhysRevApplied.11.034068>
15. J.K. Lim, P. Frigola, G. Travish et al., Adjustable, short focal length permanent-magnet quadrupole based electron beam final focus system. *Phys. Rev. Spec. Top. Accel. Beams* **8**, 072401 (2005). <https://doi.org/10.1103/PhysRevSTAB.8.072401>
16. R.K. Li, P. Musumeci, Single-shot MeV transmission electron microscopy with picosecond temporal resolution. *Phys. Rev. Appl.* **2**, 024003 (2014). <https://doi.org/10.1103/PhysRevApplied.2.024003>
17. K. Halbach, Permanent multipole magnets with adjustable strength. *IEEE Trans. Nucl. Sci.* **30**, 3 (1982). <https://doi.org/10.1109/TNS.1983.4336645>
18. T. Mottershead, D. Barlow, B. Blind et al., Design and operation of a proton microscope for radiography at 800 MeV. *Proceedings of the 2003 Particle Accelerator Conference*, vol. 1, 702–704 (2003). <https://doi.org/10.1109/PAC.2003.1289014>
19. S. Becker, M. Bussmann, S. Raith et al., Characterization and tuning of ultrahigh gradient permanent magnet quadrupoles. *Phys. Rev. Spec. Top. Accel. Beams* **12**, 102801 (2009). <https://doi.org/10.1103/PhysRevSTAB.12.102801>
20. R.D. Brown, J.R. Cost, Radiation effects in magnetic and superconducting materials. *JOM* **42**, 39–43 (1990). <https://doi.org/10.1007/BF03220872>
21. E.W. Blackmore, Radiation effects of protons on samarium-cobalt permanent magnets. *IEEE Trans. Nucl. Sci.* **32**, 3669–3671 (1985). <https://doi.org/10.1109/TNS.1985.4334463>
22. D. Cesar, J. Maxson, P. Musumeci et al., Demonstration of single-shot picosecond time-resolved MeV electron imaging using a compact permanent magnet quadrupole based lens. *Phys. Rev. Lett.* **117**, 024801 (2016). <https://doi.org/10.1103/PhysRevLett.117.024801>
23. H. Chen, L. Yan, Q. Tian et al., Commissioning the photoinjector of a gamma-ray light source. *Phys. Rev. Accel. Beams* **22**, 053403 (2019). <https://doi.org/10.1103/physrevaccelbeams.22.053403>
24. P.W. Hawkes, *Quadrupoles in Electron Lens Design* (Academic Press, London, 1970), New York
25. Y. Zhao, Z. Zhang, W. Gai et al., High energy electron radiography scheme with high spatial and temporal resolution in three dimension based on a e-LINAC. *Laser Part. Beams* **34**, 338–342 (2016). <https://doi.org/10.1017/s0263034616000124>
26. K. Makino, M. Berz, Cosy infinity version 9. *Nucl. Instrum. Method A* **558**, 346–350 (2006). <https://doi.org/10.1016/j.nima.2005.11.109>
27. S. Agostinelli, J. Allison, K. Amako et al., Geant4-a simulation toolkit. *Nucl. Instrum. Method A* **506**, 250–303 (2003). [https://doi.org/10.1016/S0168-9002\(03\)01368-8](https://doi.org/10.1016/S0168-9002(03)01368-8)
28. K. Floettmann, ASTRA, DESY, <https://www.desy.de/~mpyflo/>
29. J. Xiao, Z. Zhang, S. Cao et al., Areal density and spatial resolution of high energy electron radiography. *Chin. Phys. B* **27**, 035202 (2018). <https://doi.org/10.1088/1674-1056/27/3/035202>
30. J.H. Xiao, Y.C. Du, H.Q. Li et al., Ultrafast high energy electron lens radiography suitable for transient electromagnetic field diagnosis. *J. Instrum.* **17**, P01033 (2022). <https://doi.org/10.1088/1748-0221/17/01/p01033>
31. Z. Zhou, Research on high spatiotemporal resolution high energy electron imaging and electron diffraction. *Dissertation*. (2019). <https://doi.org/10.27266/d.cnki.gqhau.2019.000630>(in Chinese)
32. L. Zheng, J. Shao, Y. Du et al., Overestimation of thermal emittance in solenoid scans due to coupled transverse motion. *Phys. Rev. Accel. Beams* **21**, 122803 (2018). <https://doi.org/10.1103/physrevaccelbeams.21.122803>
33. G. Manahan, E. Brunetti, C. Aniculaesei et al., Characterization of laser-driven single and double electron bunches with a permanent magnet quadrupole triplet and pepper-pot mask. *New J. Phys.* **16**, 103006 (2014). <https://doi.org/10.1088/1367-2630/16/10/103006>

Springer Nature or its licensor (e.g. a society or other partner) holds exclusive rights to this article under a publishing agreement with the author(s) or other rightsholder(s); author self-archiving of the accepted manuscript version of this article is solely governed by the terms of such publishing agreement and applicable law.